Published in final edited form as:
NMR Biomed. 2014 November ; 27(11): 1313–1324. doi:10.1002/nbm.3191.

Advantages of Chemical Exchange-Sensitive Spin-Lock (CESL) Over Saturation Transfer (CEST) for Hydroxyl- and Amine-Water Proton Exchange Studies

Tao Jin[1] and **Seong-Gi Kim**[1,2,3]

[1]Neuroimaging Laboratory, Department of Radiology, University of Pittsburgh, Pittsburgh, Pennsylvania, USA

[2]Center for Neuroscience Imaging Research, Institute for Basic Science (IBS), Suwon, Korea

[3]Departments of Global Biomedical Engineering and Biological Sciences, Sungkyunkwan University, Suwon, Korea

Abstract

The chemical exchange (CE) rate of endogenous hydroxyl and amine protons with water is often comparable to the difference in their chemical shifts. These intermediate exchange (IMEX) processes have been imaged by the CE saturation transfer (CEST) approach with low-power and long-duration irradiation. However, its sensitivity is not optimal, and more importantly, the signal is contaminated by slow magnetization transfer processes. Here, the property of CEST signals is compared to a CE-sensitive spin-locking (CESL) technique irradiating at the labile proton frequency. Firstly, using a higher power and shorter irradiation in CE-MRI yields i) increasing selectivity to faster chemical exchange rates by higher sensitivity to faster exchanges and less sensitivity to slower CE and magnetization transfer processes, and ii) decreasing *in vivo* asymmetric magnetization transfer contrast measured at ±15 ppm. The sensitivity gain of CESL over CEST is higher for a higher-power and shorter irradiation. Unlike CESL, CEST signals oscillate at a very high power and short irradiation. Secondly, time-dependent CEST and CESL signals are well modeled by analytical solutions of CE-MRI with asymmetric population approximation (CEAPA), which can be used for quantitative CE-MRI, and validated by simulations of Bloch-McConnell equations and phantom experiments. Lastly, *in vivo* amine-water proton exchange contrast measured at 2.5 ppm with ω_1 of 500 Hz is 18% higher in sensitivity for CESL than CEST at 9.4 T. Overall, CESL provides better exchange rate selectivity and sensitivity than CEST; therefore, CESL is more suitable for CE-MRI of IMEX protons.

Keywords

chemical exchange; CEST; CESL; hydroxyl; amine; sensitivity; selectivity

*Corresponding author: Tao Jin, Ph. D., Department of Radiology, University of Pittsburgh, 3025 E Carson Street, Room 156, Pittsburgh, PA, 15203, taj6@pitt.edu, (Tel) 412-383-8010, (Fax) 412-383-6799.

Introduction

The chemical exchange (CE) process provides novel MRI contrasts to probe tissue pH, mobile proteins, and many metabolites and has gained increasing interest in preclinical and clinical studies, such as stroke, tumor, and cartilage degeneration (1–9). The CE-MRI contrast is generally studied by a chemical exchange saturation transfer (CEST) technique (10), in which biomolecules are indirectly detected by the reduction of water magnetization after their selectively irradiated labile protons exchange with water. In most previous CEST studies, the CE falls into the slow-exchange regime; *i.e.*, the exchange rate (k) $\ll$ the resonance frequency separation (δ) between water and labile protons, such as studies of the endogenous amide-water proton transfer (APT) effect (1,3,6), as well as many paramagnetic CEST agent applications (11–15). Recently, endogenous CEST has been extended to studies of other proton exchanges, such as the hydroxyl-water exchange from glycogen, glycosaminoglycan, glucose, and myo-inositol (16–23) or the amine-water proton exchange from amino acids, creatine, and mobile protein side chains (24–27). Under commonly used magnetic field strengths (3 T to 11.6 T), many of these exchange processes fall into the intermediate-exchange (IMEX) regime (roughly, $1/3 < k/(2\pi\delta) < 3$, with k and δ in s^{-1} and Hertz units, respectively).

In CEST, effective saturation of faster-exchanging labile protons requires higher irradiation power. However, because the resonance frequencies of endogenous hydroxyl and amine protons are close to water (being ~1–3 ppm), the applicable irradiation power is limited by direct water saturation (DWS) (10). Thus, IMEX-CEST studies have adopted relatively low-power and long-duration off-resonance irradiation (16,18,20,26), which is known to be optimal for slow exchange applications. As such, the sensitivity of IMEX-CEST is not optimized. More importantly, the IMEX signal can not be effectively separated from confounding CEST signals with overlapping frequencies and slow exchange rates, such as the APT signal (1). Additionally, the IMEX signal will be contaminated by the nuclear Overhauser enhancement (NOE) signal from aliphatic protons of mobile protein/lipids (7,17,28–32) and the *in vivo* asymmetric magnetization transfer contrast (MTC) from semisolid macromolecules when conventional asymmetric analysis is applied. An alternative chemical exchange-sensitive spin-locking (CESL) technique can suppress the DWS (33,34), yielding much wider freedom in the selection of irradiation parameters. Specifically, the choice of much-higher-power and shorter-duration irradiation becomes possible, which can be exploited to improve the sensitivity and/or exchange rate selectivity of IMEX signals. While some promising results have been reported regarding these aspects (25,33), a more systematic comparison of the two techniques and experimental validation are necessary.

Although the CE process can be well described by the Bloch-McConnell equations, an analytical description of the IMEX signal can provide more insight to understand the signal properties, to optimize imaging contrast, and to determine quantitative CE parameters, such as the exchange rate and the biomolecule concentrations. Note that the IMEX signal can not be described by current CEST theoretical models, which were developed in the slow exchange regime (7,24,35–38). To take full advantage of the freedom in the selection of irradiation parameters, it is preferable to have an analytical description of IMEX signals, which may be achieved by the recent model for CE-sensitive MRI under asymmetric

population approximation (CEAPA) (33,39). We have applied the steady-state CEAPA solutions to both CEST and CESL MRI for characterizing Z-spectra, hence determining the exchange rate and metabolite concentration (33). Although we have also derived time-dependent CEAPA analytical solutions (40), these solutions were not experimentally confirmed for IMEX applications.

In this work, irradiation time-dependent CEST and CESL signals were simulated by the Bloch-McConnell equations and measured in phantoms with multiple irradiation powers for IMEX protons and compared with analytical CEAPA solutions. Then, the sensitivity and exchange rate selectivity of CEST and CESL were determined, and the accuracy of the CEAPA solutions was examined. The sensitivity advantage of CESL over CEST and the capability of minimizing *in vivo* asymmetric MTC with high-power and short-duration irradiation were validated by *in vivo* experiments in normal and ischemic rat brain. Part of the results have been reported in a recent meeting (19).

Theoretical background

Assuming that the population of exchanging pools is highly asymmetric (*i.e.*, the water pool is much larger than others), Trott and Palmer reported the longitudinal relaxation rate in the rotating frame for a two-pool chemical exchange (39) and then extended it to multi-pool exchange (41). We have applied this relaxation model and derived time-dependent analytical solutions for both CEST and CESL MRI signals (25,33,40). Similar solutions have also been obtained by other groups (34,42).

Exchange-mediated relaxation

Chemical exchange between labile protons and water protons can be sensitized by off-resonance continuous-wave irradiation with a radiofrequency (RF) offset of Ω from water, a Rabi frequency of ω_1 (= $\gamma B_1/2\pi$), and duration of t_{irrad}. The relaxation of water proton magnetization under $B_{1,\mathrm{eff}}\,(=2\pi\sqrt{\Omega^2+\omega_1^2}/\gamma)$ can be decomposed into two components: one parallel to the $B_{1,\mathrm{eff}}$ direction is the longitudinal relaxation rate in the rotating frame ($R_{1\rho}$), and one perpendicular to the $B_{1,\mathrm{eff}}$ direction is the transverse relaxation rate in the rotating frame ($R_{2\rho}$). Due to inhomogeneities in B_0 and B_1, in practice, the *apparent* $R_{2\rho}$ relaxation rate is much faster than $R_{1\rho}$. In multiple-pool exchange systems, provided that all non-water exchanging pools are small and their exchange is predominantly with water, $R_{1\rho}$ can be expressed as (41):

$$R_{1\rho}=R_1\cdot\cos^2\theta+(R_2+\sum_i R_{ex,i})\cdot\sin^2\theta, \quad [1]$$

where θ = arctan(ω_1/Ω) is the angle between $B_{1,\mathrm{eff}}$ and B_0, R_1 and R_2 are the longitudinal and transverse relaxation rates of water protons excluding the CE effect, and $R_{ex,\,i}$ is the exchange-mediated relaxation rate between water and the *i*-th labile proton pool. Assuming that the labile proton concentration is much smaller than water and their R_1 and R_2 relaxation rates are much slower than the exchange rates, R_{ex} from each individual labile proton pool can be expressed as (41):

$$R_{ex} \approx \frac{4\pi^2 \cdot P_S \cdot k \cdot \delta^2}{4\pi^2(\delta-\Omega)^2+4\pi^2\omega_1^2+k^2}, \quad [2]$$

where δ is the separation of labile proton resonance from water proton frequency and P_S is the ratio of labile proton to water proton concentration. The factors of $4\pi^2$ in Eq. [2] take into account that the units of Ω, δ, and ω_1 are commonly used as Hz (= 2π·rad/s), while the unit of relaxation rates and k is s^{-1}.

CE-sensitive MRI with saturation transfer vs. spin-lock

In the simplest case, a CEST or CESL preparation has a continuous-wave off-resonance RF irradiation that induces an effective $B_{1,eff}$, tilted at an angle θ from the B_0 direction (33). With CESL, there are two additional on-resonance hard pulses: one flips the water magnetization from the Z-axis to $B_{1,eff}$ direction before the off-resonance irradiation for the spin-lock (SL), and the other flips the water magnetization back to the Z-direction after SL for imaging. When the magnetization component perpendicular to the $B_{1,\,eff}$ dephases instantaneously (*apparent* $R_{2\rho} \rightarrow \infty$), the normalized magnetization at the RF offset of Ω has been derived as (25,40,42):

$$S_{irrad}(\Omega)/S_0 = \left\{[\cos(\lambda\theta)-S_{SS}] \cdot e^{-R_{1\rho}\cdot t_{irrad}}+S_{SS}\right\} \cdot \cos(\lambda\theta) \quad [3]$$

where *irrad* = CEST or CESL irradiation, and $S_{SS} = (R_1 \cdot \cos\theta/R_{1\rho})$ is the normalized steady-state signal along the $B_{1,eff}$ direction. λ represents the relative error of the SL, which equals 0 for ideal SL and 1 for CEST, because CEST can be considered an approximation of CESL without SL flip pulses (33,40). The λ term is equivalent to $(1 - \phi/\theta)$, where ϕ is the actual flip angle of the on-resonance flip pulses (40). Such error can be due to imperfectness in B_1 and/or B_0. The signal intensity of CEST is lower than that of CESL by a projection factor of $\cos\theta$ at the steady state when $t_{irrad} \cdot R_{1\rho} \gg 1$ and by $\cos^2\theta$ at very short irradiation (i.e., $t_{irrad} \cdot R_{1\rho} \ll 1$). The CE-sensitive images are typically obtained by so-called asymmetry analysis, from the difference in the normalized signal intensities of two images at the label ($\Omega = +\delta$) and reference ($\Omega = -\delta$) frequencies, which is referred to as the asymmetry of the magnetization transfer ratio (MTR_{asym}) for CEST and the spin-lock ratio (SLR_{asym}) for CESL. The ratio of SLR_{asym} to MTR_{asym} approaches $1/\cos^2\theta$ at very short t_{irrad} and $1/\cos\theta$ at the steady state, similar to the ratio of S_{CESL} to S_{CEST}.

Materials and Methods

Simulations

Numerical solutions of Bloch-McConnell equations and the analytical CEAPA equations (Eqs. [1]–[3]) were performed using Matlab 7.0® (MathWorks, Natick, MA) Two-pool exchange was simulated to compare the sensitivity of CESL versus CEST and to validate analytical CEAPA solutions. The default parameters assumed in the simulations were $\delta = 1$ ppm (400 Hz or 2510 rad/s at 9.4 T), $k = 1500\ s^{-1}$, $R_1 = 0.35\ s^{-1}$, and $P_S = 0.001$ if not specified otherwise, and the R_1 and R_2 values of the labile proton were assumed to be the same as water. S_{CEST} and S_{CESL} at $\Omega = \pm\delta$ were simulated with the CEAPA solutions for

five ω_1 values from 50 to 400 Hz for R_2 of 3 and 25 s^{-1}, and MTR_{asym} and SLR_{asym} were calculated as $[S(-\delta)- S(+\delta)]/S_0$. R_2 of 3 s^{-1} is closer to that of aqueous phantom, and R_2 of 25 s^{-1} is due to *in vivo* T_2 of 40 ms at 9.4 T (43). A power of SL flip pulse was chosen as 500 Hz, and the duration was calculated so that the flip angle equals θ(= arctan(ω_1/Ω)).

To mimic actual experimental conditions, two additional situations were simulated. First, to evaluate CEAPA solutions for CEST, the RF offset of a labile proton was assumed to be equally distributed between Ω = 390 Hz to 410 Hz for the condition in the presence of small B_0 inhomogeneity of 20 Hz. Specifically, water magnetization was divided into 101 parts with a B_0 shift of −10 to 10 Hz in 0.1-Hz steps. The time evolution of the magnetization vector of each part was calculated by Bloch equations and added together. Secondly, to estimate the effect from the imperfect SL due to B_1 and/or B_0 inhomogeneity, an error of SL λ was assumed, so that the magnetization would be flipped to the cone with an angle of $\lambda\theta$ with $B_{1,\,eff}$ direction by the first flip pulse and flipped back after SL to the cone with an angle of $\lambda\theta$ with the Z-axis. λ was simulated for selected values between 0.0 (ideal CESL) to 1.0 (ideal CEST).

To compare the dependence of IMEX versus confounding slow exchange CE-MRI signals on irradiation parameters, four-pool exchanges were simulated assuming the magnetization of water proton exchanges with amine, amide, and aliphatic proton magnetization. While the *in vivo* aliphatic NOE signals are upfield from water (*i.e.*, negative RF offset), they affect the IMEX CE-MRI signal through the asymmetry analysis. To generate a similar magnitude observed *in vivo* at 9.4 T, we assumed that R_1 = 0.5 s^{-1} and R_2 = 25 s^{-1} as water relaxation rates; k_{amine} = 7500 s^{-1}, δ_{amine} = 1200 Hz (3 ppm), and P_{amine} = 0.0012 for the amine pool; k_{amide} = 30 s^{-1}, δ_{amide} = 1400 Hz, and P_{amide} = 0.0012 for the amide pool (44); and $k_{aliphatic}$ = 20 s^{-1}, $\delta_{aliphatic}$ = −1200 Hz, and $P_{aliphatic}$ = 0.003 for the aliphatic pool. SLR_{asym} was calculated with the CEAPA solutions as a function of irradiation power and duration at Ω = ±1200 Hz. The selectivity of amine signals was evaluated by an index of contaminations from slow-exchanging protons, which was calculated as $\varepsilon_i = |SLR_{asym}(i)|/SLR_{asym}(amine)$, where *i* represents amide and/or aliphatic protons. The selectivity is highest when the contamination index approaches 0.

MR experiments and data analysis

All phantom and animal MRI experiments were performed on a 9.4-T horizontal-bore magnet. A 38-mm inner diameter volume coil (Rapid Biomedical, Ohio) was used for phantom experiments, while a detunable volume excitation and surface receiver coil combination (Nova Medical, MA, USA) was used for animal studies. Before the CEST and CESL experiments, T_1 map was obtained using an inversion-recovery sequence, B_1 field was mapped for calibration of the transmit power (13), and B_0 map was obtained using the water saturation shift referencing scheme to evaluate the field homogeneity (45). The pulse sequence for CEST and CESL MRI has been described previously (9), where the CE contrast was first generated by a CEST or CESL preparation, and then, images were acquired with a spin-echo echo-planar imaging (EPI) technique. To normalize CE-sensitive signals, S_0 images were acquired at an offset frequency of 300 ppm.

Phantom experiments

Phantoms were imaged with a field of view = 4 × 4 cm^2, matrix size = 64 × 64, slice thickness = 5 mm, echo time (TE) = 30 ms, and repetition time (TR) = 16 s. Four sets of experiments were performed at room temperature.

i. To evaluate the difference in saturation transfer (ST) and SL signal sensitivity due to DWS, 2% (by weight) agar phantom was used, where there is no CE effect. ST and SL images were acquired for irradiation times from 0 to 4 s, with a fine step of 5 ms in the initial 80 ms, at a frequency offset of 400 Hz and three ω_1 values of 100, 200, and 400 Hz. Two different field inhomogeneity conditions were compared: a highly homogeneous condition with a water line width of 6 Hz and a more inhomogeneous condition, where the shimming was modified to give a water line width of 46 Hz.

ii. To compare the CEST and CESL signals in the intermediate exchange regime, 50 mM myo-inositol (Ins, cyclohexane-1,2,3,4,5,6-hexol, $\underline{C}_6\underline{H}_{12}\underline{O}_6$) containing hydroxyl groups was dissolved in phosphate-buffered saline (PBS, pH = 7.4) containing 10 mM of phosphate buffer. MTR_{asym} and SLR_{asym} were measured at 1 ppm with six ω_1 values of 70, 100, 141, 200, 282, and 400 Hz. For each ω_1, irradiation times were varied from 0 up to 6 s. In addition, on-resonance $R_{1\rho}$ dispersion was measured for 11 ω_1 values from 125 to 2828 Hz. By fitting the on-resonance $R_{1\rho}$ dispersion data to Eqs. [1] and [2], P_S, R_2, δ, and k values were obtained. Together with the measured R_1 value, S_{CEST} and S_{CESL}, as a function of t_{irrad} and ω_1, were simulated for Ω = +1 and −1 ppm using Eq. [3], respectively, from which MTR_{asym} and SLR_{asym} were calculated as $[S(-1\text{ ppm}) - S(+1\text{ ppm})]/S_0$ and compared with the experimental data.

iii. To examine whether the CEAPA solution also works for conditions closer to tissue, 50 mM Ins in PBS was also mixed in 0.7%, 1%, 2%, and 3% agar gel. SLR_{asym} at 1 ppm was measured with ω_1 = 160 Hz and 21 t_{irrad} values, ranging from 0 to 2 s in a 0.1-s step. In Eq. [1], the addition of agar increases the water R_2 and also introduces a relaxation term, R_{MT}, due to the magnetization transfer effect. The effective water R_2 ($R_{2,\,eff} = R_2 + R_{MT}$) values of these mixtures were measured by on-resonance SL experiments with a SL frequency of 4000 Hz to suppress the CE effect (40). Additionally with the P_S, δ, and k values previously obtained from Phantom Expt (ii), MTR_{asym} and SLR_{asym} were calculated and compared with the experimental data.

iv. To demonstrate that higher-power SL irradiation improves the selectivity of IMEX versus slow CE signals, four phantoms in PBS with a pH of 7.4 and 0.15 mM $MnCl_2$ were PBS-only, and three metabolites: 30 mM glutamate (Glu) containing a primary amine group with a chemical shift difference of 3 ppm from water, 200 mM nicotinamide (Nic) containing two amide groups with 3.4- and 2.6-ppm offsets from water, and 30 mM Glu together with 200 mM Nic. CESL Z-spectrum was measured with ω_1 = 120 Hz and 4 s, and SLR_{asym} at 3 ppm was measured with ω_1 = 240 Hz for t_{irrad} values up to 2 s and with ω_1 = 750 Hz for t_{irrad} values up to 0.4 s.

In vivo experiments

Thirteen male Sprague-Dawley rats were studied with approval by the Institutional Animal Care and Use Committee at the University of Pittsburgh. Six animals were for *in vivo* asymmetric MTC studies, 3 were for time-dependent CESL and CEST behavior, and 4 were for the CEST versus CESL comparison of ischemic contrast. The animals were anesthetized with isoflurane (5% for induction and 2% during surgery) in a mixture of O_2 and air gases, with the O_2 concentration kept at 30% throughout the experiment. The right femoral vein and artery were catheterized to deliver maintenance fluid and to monitor the arterial blood pressure, respectively. In four animals, a middle cerebral arterial occlusion was carried out to induce pH-reducing permanent ischemia in the left hemisphere (46). After surgery, the isoflurane level was reduced to 1.3%–1.5% during MRI scans. The dynamic blood pressure and end-tidal CO_2 were monitored. End-tidal CO_2 level was kept within 3.0% and 4.0%, and the rectal temperature was maintained at 37.0 ± 0.5°C using a feedback-controlled heating pad.

All *in vivo* CE-MRI images were acquired by the spin-echo EPI sequence with a field of view = 3.2 × 3.2 cm^2, matrix size = 64 × 64, TE = 28 ms, slice thickness = 2 mm, and four consecutive slices without gap. Three *in vivo* experiments were performed.

i. To evaluate the dependence of *in vivo* asymmetric MTC on irradiation parameters, MTR_{asym} was measured in rat brains at ±15 ppm (n = 6) with TR = 10 s and calculated as $[S(-15\text{ ppm}) - S(+15\text{ ppm})]/S_0$. Because asymmetric MTC extends to a wide frequency range (47), a large offset of 15 ppm was chosen to minimize contaminations from direct water saturation, as well as CE and NOE effects. Four irradiation power and duration pairs, which have been recently applied in hydroxl- and amine-water exchange studies, were compared: ω_1 = 63 Hz for 4 s (20,23), 150 Hz for 2 s (48), 250 Hz for 1 s (49), and 500 Hz for 0.15 s (25,50). To compare the quantitative data in gray and white matter, regions of interest (ROIs) were selected in the cortex and the corpus callosum area.

ii. Amine-water proton exchange (APEX)-sensitive CEST and CESL measurements were performed at 2.5 and −2.5 ppm with continuous-wave ω_1 of 500 Hz, t_{irrad} between 0 and 500 ms (25), and TR = 7 s. This offset was chosen, because for the fast amine-water proton exchange, the frequency of specificity/selectivity reduces, and the CE signal can be detected with similar sensitivity by adjusting ω_1 and t_{irrad} (25). To examine whether the CESL results are sensitive to inaccurate spin-locking due to B_1 and B_0 inhomogeneities, CESL data of normal animals (n = 3) were also acquired with a 30% error in the flip angle of on-resonance flip pulses (*i.e.*, λ = 0.3), without changing the long off-resonance irradiation pulse.

iii. The same APEX parameters shown above in *In Vivo* Expt (ii) were used to compare the ischemic contrast of CEST versus CESL. To identify ischemic regions in stroke animals (n = 4), ADC maps were obtained using a spin-echo EPI sequence without diffusion-weighting and with a diffusion-weighting *b* value of 1200 s/mm^2 along six different directions. In the ischemic animals, MTR_{asym} and SLR_{asym} maps were obtained. An ischemic ROI, with about 2 × 2 mm^2 in one slice, was selected from the ADC map, and a control ROI was chosen in the same brain region

contralateral to the ischemic ROI. Then, MTR_{asym} and SLR_{asym} were compared as a function of irradiation time from 0 to 500 ms.

Results

Sensitivity of CEST vs. CESL MRI: Simulations and Phantom Studies

Time-dependent magnetization was simulated using Bloch-McConnell equations with 150 Hz irradiation applied at 1 ppm (Fig. 1). The CESL signal is dependent on the error of the flip pulses, λ (Fig. 1A). For λ = 1, the simulated CESL signal is the same as the CEST signal, while λ of 0 is for the ideal CESL condition. At a short t_{irrad}, CEST shows a significant signal oscillation, as expected (33,42,51,52). When λ decreases from 1.0 to 0.0 (*e.g.*, on-resonance flip angle increases from 0 to θ), the signal intensity increases with reduced oscillations. For λ ≤ 0.5, the CESL signal is already fairly close to that of the ideal CESL. With the presence of field inhomogeneity, the apparent $R_{2\rho}$ relaxation increases, so that the oscillation quickly disappears (Fig. 1B), and the Bloch-McConnell simulation results match well with the CEAPA solutions for both CEST and CESL. To experimentally confirm the simulation data, saturation transfer and spin-locking MRI of 2% agar phantoms were measured at 1 ppm with ω_1 = 100, 200, and 400 Hz for a water spectral line width of 6 Hz and 46 Hz. Consistent with the simulation data (Fig. 1A and B), the t_{irrad}-dependent ST MRI signal oscillation is clear when the field homogeneity is high (Fig. 1C) but disappears quickly with large field inhomogeneity (Fig. 1D).

Fig. 2 compares the optimal ω_1 and t_{irrad} values for CESL with R_2 of 25 s^{-1} for three exchange rates: k = 100 s^{-1} (A), 1500 s^{-1} (B), and 5000 s^{-1} (C). Overall, CE-MRI is much more sensitive in the slow exchange regime, and the maximal SLR_{asym} is reduced for k = 5000 s^{-1} (k/δ = 2) than k = 1500 s^{-1} (k/δ = 0.6). With increasing k, the optimal CE sensitivity occurs at higher ω_1 and shorter t_{irrad}. The ratio of SLR_{asym} to MTR_{asym} is nearly independent of k value and is shown in Fig. 2D, which is larger at higher ω_1 and shorter t_{irrad}.

To further compare CESL and CEST sensitivity in the IMEX regime, MTR_{asym} (dashed line) and SLR_{asym} (solid line) were simulated using CEAPA analytical solutions for k = 1500 s^{-1} with R_2 of 3 s^{-1} (Fig. 3A and 3B) and 25 s^{-1} (Fig. 3C and 3D). Three observations were noted. i) Compared to R_2 of 3 s^{-1}, the CE signal with a larger R_2 of 25 s^{-1}, measured by both MTR_{asym} and SLR_{asym}, is reduced due to the increased $R_{1\rho}$ (but the same R_{ex}, see Eq. [1]), and the CE signal peaks at lower ω_1 (Fig. 3C vs. 3A). ii) At ω_1 of 50 Hz, MTR_{asym} and SLR_{asym} are nearly identical and increase with t_{irrad}. With increasing ω_1, the peaks of MTR_{asym} and SLR_{asym} shift to smaller t_{irrad} values, because the CE contrast is additionally affected by the increase of ω_1 (or θ) due to the $\cos\theta$ term (see Eq. [3]). iii) With the same irradiation parameters, SLR_{asym} is always higher than MTR_{asym}, and the difference increases with ω_1. The ratio of SLR_{asym} to MTR_{asym} approaches $1/\cos^2\theta$ at very short t_{irrad} and $1/\cos\theta$ at the steady state (Figs. 3C and 3D).

To confirm our CEAPA simulation data with experimental data, MTR_{asym} and SLR_{asym} of 50 mM Ins in PBS were measured at six ω_1 levels and are shown in Fig. 3E–F for three different ω_1. Peaks of MTR_{asym} and SLR_{asym} shifted to shorter t_{irrad} with increasing ω_1. For

the same ω_1, SLR_{asym} is always higher than MTR_{asym}, and the SLR_{asym}/MTR_{asym} ratio increases with increasing ω_1 and shorter t_{irrad} (Fig. 3F), similar to the prediction from the CEAPA solutions (see Fig. 3B).

CEAPA Solutions vs. Tissue-Mimicking Phantom Data

To examine whether CEAPA solutions can explain the experimental irradiation time-dependent MTR_{asym} and SLR_{asym} data in the Ins phantom (Fig. 3E), $P_S = 0.003$, $\delta = 370$ Hz (2323 rad/s), $k = 1250\ s^{-1}$, and $R_2 = 0.4\ s^{-1}$ were obtained by fitting on-resonance $R_{1\rho}$ dispersion data with Eqs. [1] and [2] (19). Using these fitted values of Ins (except for an R_2 of $0.5\ s^{-1}$, which gives a better match than $0.4\ s^{-1}$) and a measured R_1 of $0.35\ s^{-1}$, irradiation time-dependent MTR_{asym} and SLR_{asym} were simulated (Fig. 3E, lines). Both MTR_{asym} and SLR_{asym} simulation data (lines) matched well with the experimental data (symbols).

To further examine whether the CEAPA solutions apply to conditions closer to *in vivo*, we measured the SLR_{asym} (symbols in Fig. 4), R_1, and R_2 of four Ins samples with different agar concentrations. With increasing agar concentration, SLR_{asym}, as well as the peak t_{irrad}, decreased. The water $R_{2,\,eff}$ value is nearly proportional to the agar concentration, being 4.02, 5.97, 12.50, and $18.08\ s^{-1}$ for 0.7%, 1%, 2%, and 3% agar samples, respectively. In contrast, the water R_1 value only very weakly increases with agar concentration, being 0.35, 0.36, 0.37, and $0.38\ s^{-1}$ for these samples. Using the aforementioned fitted results of Ins and the measured R_1 and $R_{2,\,eff}$ values, SLR_{asym} can be predicted from Eq. [3] (solid lines in Fig. 4), which match well with the experimental data for all four samples (symbols in Fig. 4). Thus, these results indicate that CEST and CESL data can be well explained by the analytical CEAPA solutions for both aqueous and tissue-mimicking systems.

Exchange Rate Selectivity of CE-MRI to IMEX Protons

Due to their overlapping frequencies, the *in vivo* IMEX MTR_{asym} or SLR_{asym} signal contains contaminations from both amide and aliphatic protons (28,31,32,53). Besides the sensitivity enhancement, another major benefit of using higher irradiation power is sensitizing faster exchange processes, as can be seen in Fig. 2A–C. To demonstrate this property, SLR_{asym} at 3 ppm was simulated as a function of irradiation power and duration for an amine pool, an amide pool, an aliphatic pool, and the combination of all three pools (Fig. 5A–D). The amide signal is slightly positive, whereas the aliphatic proton signal is largely negative. With low-power and long-duration irradiation, the negative SLR_{asym} is dominated by the contribution from aliphatic protons, whereas with high-power and short-duration irradiation, the positive SLR_{asym} is dominated by the contribution from amine protons (Fig. 5D). This is very similar to our observations *in vivo* (25).

The contamination of amide and aliphatic protons to the amine CE signal was shown in Fig. 5E–G. If ε ($=|SLR_{asym}(\text{non-amine})|/SLR_{asym}(\text{amine})$) = 0, then there is no contamination. At a high irradiation power, such as >400 Hz, the contamination of amide and hydroxyl protons is minimal. Compared to SLR_{asym} which is sensitive to both ω_1 and t_{irrad} (Fig. 2A–C and 5A–D), the index of contamination ε is mainly determined by ω_1 and is only weakly dependent on t_{irrad}. This indicates that the exchange rate selectivity is mainly determined by

the irradiation power, whereas the selection of t_{irrad} is important for the optimization of sensitivity.

The selectivity of IMEX versus slow exchange by ω_1 was demonstrated in phantoms. Amide proton was chosen for this purpose, given the difficulty of constructing phantoms with the aliphatic NOE effect only. In Fig. 6A, the Z-spectra and the SLR_{asym} of Glu and Nic phantoms showed that the CESL signals of amine and amide protons are overlapping. With a relatively low ω_1 of 120 Hz, the SLR_{asym} signal from Nic with amide protons is higher than that of Glu with amine protons at 3 ppm — the offset frequency of amine protons. SLR_{asym} at 3 ppm of the Glu and Nic phantoms was compared for two higher ω_1 values. With a medium ω_1 of 240 Hz, Glu and Nic have similar CE sensitivity, with peaks at t_{irrad} > 1 s (Fig. 6B). When ω_1 was increased to 750 Hz, the peak of SLR_{asym} shifted to 0.2 s or less (Fig. 6C), where the CE sensitivity of Glu is much larger than that of Nic. SLR_{asym} maps, measured at 3 ppm, are shown in Fig. 6D; both Glu and Nic contribute equally for a ω_1 of 240 Hz and t_{irrad} of 1 s, but the Glu signal is predominant for a ω_1 of 750 Hz and t_{irrad} of 0.1 s. At a large ω_1, an increase in θ (and the $R_{1\rho}$) decreases the water magnetization and, hence, the amide-CE signal (Eq. [1]). But the CE signal from Glu does not drop, because the higher ω_1 improves the saturation efficiency.

Overall, with the coexistence of slow- and intermediate-exchange species, a higher ω_1 and shorter t_{irrad} pulse can be exploited to enhance the selectivity and sensitivity to IMEX CE-MRI signals and minimize the contamination from slow-exchange protons. Note that CEST has similar selectivity properties, but a very short irradiation time can not be used because of DWS-induced signal oscillation, as shown in Figs. 1A and 1C.

Minimizing in vivo MTC asymmetry with high irradiation power

There is a concern that a higher ω_1 may induce larger MTC asymmetry from semisolid macromolecules, resulting in a larger error of MTR_{asym} for CE-MRI. To examine this issue, MTR_{asym} at 15 ppm was measured in rat brains (Fig. 7), which is dominated by the MTC asymmetry. Similar to the MTC effect, this MTC asymmetry is significantly higher in magnitude in white matter than gray matter. In general, MTC asymmetries in both the cortex (blue pixels) and corpus callosum (green pixels) decrease with higher power and shorter duration. With 500 Hz and 0.15 s, MTC asymmetry is suppressed, indicating that a high-power and short-saturation pulse is able to reduce the MTC asymmetry and increase the signal selectivity to IMEX protons.

In vivo CESL vs. CEST in the IMEX domain

Fig. 8 shows *in vivo* CEST and CESL signals measured at an RF offset of ±2.5 ppm and an ω_1 of 500 Hz, which is sensitive to amine-water proton exchange (25). In a single pixel in normal rat brain cortex (the red pixel in Fig. 8A, inset), a large oscillation was observed at t_{irrad} < 100 ms for the reference CEST images acquired at −2.5 ppm and for MTR_{asym}, but not for CESL (Fig. 8A–B). Consistent with the simulation results (Fig. 1A), a flip angle error of <0.3 is sufficient to minimize the CE-MRI signal oscillation, leading to results close to the ideal CESL (Figs. 8A and 8B). Similar signal behavior can be observed in other pixels and all animals (n = 3). Since the peak response of MTR_{asym} (and SLR_{asym}) occurs at about

100 to 200 ms (Fig. 8B), the initial fluctuation may interfere with the proper selection of irradiation time for maximizing MTR_{asym}. For t_{irrad} = 150 ms, the whole brain-averaged SLR_{asym} is 18% higher than MTR_{asym} and is 15% higher with $\lambda = 0.3$ (see Fig. 8B). While CESL significantly improves the sensitivity to MTR_{asym}, this enhancement is not due to the additional asymmetric MTC caused by the two flip pulses. With $t_{irrad} = 0$, SLR_{asym} is only $-0.07 \pm 0.15\%$ (n = 3).

In ischemic rats, the ischemic lesion area can be observed easily in both the SLR_{asym} and MTR_{asym} maps obtained with a ω_1 of 500 Hz and t_{irrad} = 150 ms (Fig. 8C), but the SLR_{asym} intensity was larger than MTR_{asym}. This ischemic contrast is mainly due to the APEX-weighted signal at the 2.5 ppm, because a negative contrast can be detected at this RF offset but not at the reference frequency of −2.5 ppm. To examine t_{irrad}-dependent CE-MRI signals, two ROIs were chosen: an ipsilaterial ischemic region selected from the ADC map and a contralateral normal region. Both MTR_{asym} and SLR_{asym} peaked at a t_{irrad} of 150 ms for the contralateral ROI and 200–250 ms for the ipsilateral ROI (Fig. 8D). The shift in peak t_{irrad} in the ischemic ROI is likely due to a longer T_2 induced by edema and, consequently, an increased optimal irradiation duration (25). The maximum contrast between ipsi- and contra-lateral ROI occurred at t_{irrad} = 300 ms and is 4.2 ± 1.2% for MTR_{asym} and 5.0 ± 1.3% for SLR_{asym} (n = 4).

Discussions

Recent studies have broadened the spectrum of CE-MRI to a wide range of biomolecules with hydroxyl or amine groups. These hydroxyl- and amine-water exchange rates are usually between 1000–10,000 s^{-1} (2,7,9), and the chemical shifts from water are ~1–3 ppm, which is 800–2500 rad/s at 3 T and 2500–7500 rad/s at 9.4 T, respectively. Therefore, many of these proton exchanges fall into the IMEX regime. While most of these IMEX studies adopted the conventional CEST approach of irradiation with a long duration (>1s) and relatively low power (~40 to ~150 Hz) (16–18,20,22,23,26,49), our results show that such a choice of irradiation parameters is not optimal. A simple addition of two on-resonance flip pulses to convert CEST to CESL acquisition can suppress the DWS and provide important benefits. Namely, with the CESL technique, irradiation parameters can be optimized in a much wider range, so that sensitivity and/or selectivity of IMEX CE-MRI signals can be improved.

Improve the IMEX Sensitivity: CEST vs. CESL

The sensitivity of CE-MRI is closely dependent on the rate of chemical exchange (slow vs. intermediate exchange) as well as imaging parameters. In CEST, the sensitivity is approximately proportional to the saturation efficiency, defined as $\alpha = \frac{\omega_1^2}{(\omega_1^2 + k^2)}$ (2,54,55). For slow-exchange applications, such as the well-studied amide proton transfer effect (56), CEST and CESL are almost identical, and the MTR_{asym} is optimal at the steady state (33). For CEST studies of hydroxyl- or amine-water proton exchange with an exchange rate of ~5000 s^{-1} (26,33), the saturation efficiency is only 2.5% for a typical ω_1 of around 125 Hz (800 rad/s) but can be increased to 28% with a ω_1 of 500 Hz. However, because amine- and

hydroxyl CE-MRI is often obtained at 2–3 ppm and ~1 ppm, respectively, an increase of the saturation efficiency induces a larger DWS effect.

For IMEX applications, a high ω_1 and short irradiation often provides optimal CE sensitivity (Fig. 2) (25,26), in which case CESL will have a higher sensitivity than CEST. In practical applications, the B_0 and B_1 inhomogeneity would lead to imperfect SL and reduce the sensitivity gain of CESL over CEST; therefore, schemes with improved SL accuracy, such as adiabatic pulses, would be beneficial. Importantly, the requirement of the accuracy of the two flip pulses in CESL is not stringent, and the sensitivity enhancement can be achieved, even with 50% error in the flip pulses. Our *in vivo* APEX studies show an 18% sensitivity gain when CESL is used and a 15% gain when the B_1 of the flip pulse is intentionally reduced by 30%. Generally, the sensitivity gain of CESL over CEST would be larger for systems for a higher ω_1 and shorter irradiation duration (Fig. 2D), which will optimize the sensitivity for a faster chemical exchange rate. Similarly, the sensitivity gain of CESL over CEST would be larger for smaller chemical shifts from water (i.e., a larger DWS effect). Therefore, the sensitivity enhancement of CESL should also be higher at lower magnetic fields, such as a clinical field of 3 T.

In addition to irradiation power and duration, the RF offset can also be adjusted in CESL, although it is only considered at the labile proton frequency in this work. From Eq. [2], the full width at a half-maximum of R_{ex} as a function of off-resonance frequency equals $2 \times \sqrt{\omega_1^2 + k^2/(2\pi)^2}$ (33). Thus, for an exchange rate k comparable to or faster than the chemical shift δ, the CE contrast can be detected in a wide range of RF offsets (see Fig. 8D in (33)). Specifically, CE-sensitive contrast can even be obtained by CESL applied on the water resonance frequency (*i.e.*, on-resonance SL), which is not possible with the CEST approach. Although the $R_{1\rho}$ of on-resonance SL has contributions from other relaxation pathways besides CE and poor chemical specificity of a certain type of labile proton, it can be applicable in a dynamic study with administered CE-sensitive agents, where the difference of $R_{1\rho}$ before and after the administration can be mostly attributed to the change of CE-sensitive agent (*e.g.*, glucose (57)).

Enhance the exchange rate selectivity: CESL with high power and short pulse

Various endogenous labile protons have similar resonance frequencies, which are close to the water resonance frequency. The amine CE-MRI has contamination from amide protons with close resonance frequencies, which is more significant for lower irradiation power (Figs. 5 and 6). Recent CEST studies have also shown large NOE signals of up to ~10% from aliphatic protons of mobile protein/lipids (28,31,32). These aliphatic protons cover a wide resonance frequency range of 0 to −5 ppm from water and therefore will affect amine as well as hydroxyl CE-MRI signals when the conventional asymmetry analysis is adopted. Another contamination to CE-MRI is the large asymmetric MTC from semi-solid macromolecules, which is very broad in a Z-spectrum due to its extremely short proton T_2, with a center of spectrum of around −2.5 ppm. Recent brain studies have shown that the magnitude of the asymmetric MTC effect is around −2% and −4% at 3 T and 9.4 T (25,47), respectively, for an irradiation power of 1–3 μT, often used for hydroxyl and amine CEST

studies. While these confounding signals cannot be separated from that of the IMEX signal, one distinct property to be exploited is their large difference in exchange rates.

With the existence of multiple exchange rates, the exchange rate selectivity can be achieved by tuning the irradiation frequency ω_1 to the targeted exchange rate (13,50). Also, long irradiation duration is preferred for slow exchange effects, which accumulate slowly. Thus, a combination of higher irradiation power and shorter duration effectively reduces the signal contributions from slow exchange processes and increases the selectivity to faster exchange processes, as shown in our phantom (Fig. 6) and *in vivo* results (Fig. 7). Due to DWS-induced oscillation in CEST at short irradiation times, the CESL approach would be a better choice. It should be noted that in the slow exchange regime, exchange rate filtering can also be achieved by a train of pulses with varied delays or varied rotation angles (58,59), in which the CE contrast may be tuned to labile protons with exchange rates of up to several hundred times per second.

Analytical model and quantification of IMEX effects

Even though $R_{1\rho}$ appears to be specific only to spin-locking experiments at first glance, it represents the longitudinal relaxation rate in the rotating frame during any on- or off-resonance RF pulses. As described in Eqs. [1] and [2], the CE-MRI signal is sensitive to both CE and non-CE-related relaxation rates. The derivation of the CE-mediated relaxation term R_{ex} (Eq. [2]) requires an assumption that the labile proton concentration is much smaller than water, which is valid for *in vivo* studies where water is the dominant pool, as compared to other biomolecules. Another assumption is that the R_1 and R_2 relaxation rates of the labile proton are much smaller than the chemical exchange rate k, which has been extended by Zaiss et al. to a more general case where R_2 can be much faster than k (42). The analytical solution (Eq. [3]) was validated by the simulation of Bloch-McConnell equations and by the close match with experimental data. These irradiation time-dependent solutions can be applied to a whole range of chemical exchange studies with slow, intermediate, or fast exchange rates and allow us to characterize CE-sensitive MR data better and optimize imaging parameters, such as irradiation power and duration, easily.

$R_{1\rho}$ is sensitive to water R_1 and R_2 of protons, as seen in Eqs. [1] and [2]. For slow exchange applications, θ is negligible and the CE effect is mostly competing with water R_1, while for IMEX studies, θ is relatively large; so, the R_2 contribution to $R_{1\rho}$ becomes significant, affecting CE-sensitive MR signals (see Fig. 3 with R_2 of 3 s^{-1} vs. 25 s^{-1}). Therefore, to quantify IMEX effects and obtain information, such as metabolite concentration or exchange rates, it is necessary to remove these non-CE components. To this end, $R_{1\rho}$ can be measured at the labile proton frequency and the reference frequency, and the non-CE relaxation rates should be cancelled or minimized by taking the asymmetry of $R_{1\rho}$ ($R_{1\rho,\,asym}$). We have recently proposed an acquisition approach, dubbed irradiation with toggling on-resonance inversion preparation, to measure $R_{1\rho}$ efficiently (40).

Conclusions

We have demonstrated that the signals of CEST and CESL MRI can be well described by analytical CEAPA solutions and that CESL MRI provides higher sensitivity and exchange

rate selectivity than CEST. Therefore, CESL would be especially valuable for hydroxyl- or amine-water proton exchange applications, which are close to the intermediate exchange regime.

Acknowledgments

This work is supported by NIH grants EB003324 and P30-NS076405.

We thank Kristy Hendrich for maintaining the 9.4 T system and Dr. Ping Wang for animal preparation.

Abbreviations used

APA	asymmetric population approximation
APEX	amine-water proton exchange
CE	chemical exchange
CEAPA	chemical exchange model with asymmetric population approximation
CESL	chemical exchange spin-lock
CEST	chemical exchange saturation transfer
DWS	direct water saturation
FWHM	full width at half maximum
IMEX	intermediate exchange
MT	magnetization transfer
MTC	magnetization transfer contrast
$\mathbf{MTR_{asym}}$	asymmetry of magnetization transfer ratio
NOE	nuclear Overhauser enhancement
PBS	phosphate-buffered saline
$\boldsymbol{R_{1\rho}}$	spin-lattice relaxation rate in the rotating frame
RF	radiofrequency
ROI	region of interest
SL	spin-lock
$\mathbf{SLR_{asym}}$	asymmetry of spin-lock ratio

References

1. Zhou JY, Payen JF, Wilson DA, Traystman RJ, van Zijl PCM. Using the amide proton signals of intracellular proteins and peptides to detect pH effects in MRI. Nat Med. 2003; 9(8):1085–1090. [PubMed: 12872167]
2. Zhou JY, van Zijl PCM. Chemical exchange saturation transfer imaging and spectroscopy. Progress in Nuclear Magnetic Resonance Spectroscopy. 2006; 48(2–3):109–136.
3. Sun PZ, Zhou JY, Sun WY, Huang J, van Zijl PCM. Detection of the ischemic penumbra using pH-weighted MRI. J Cereb Blood Flow Metab. 2007; 27(6):1129–1136. [PubMed: 17133226]

4. Zhou JY, Blakeley JO, Hua J, Kim M, Laterra J, Pomper MG, van Zijl PCM. Practical data acquisition method for human brain tumor amide proton transfer (APT) imaging. Magn Reson Med. 2008; 60(4):842–849. [PubMed: 18816868]
5. Jia GA, Abaza R, Williams JD, Zynger DL, Zhou JY, Shah ZK, Patel M, Sammet S, Wei L, Bahnson RR, Knopp MV. Amide Proton Transfer MR Imaging of Prostate Cancer: A Preliminary Study. J Magn Reson Imaging. 2011; 33(3):647–654. [PubMed: 21563248]
6. Zhou JY, Tryggestad E, Wen ZB, Lal B, Zhou TT, Grossman R, Wang SL, Yan K, Fu DX, Ford E, Tyler B, Blakeley J, Laterra J, van Zijl PCM. Differentiation between glioma and radiation necrosis using molecular magnetic resonance imaging of endogenous proteins and peptides. Nat Med. 2011; 17(1):130–U308. [PubMed: 21170048]
7. van Zijl PCM, Yadav NN. Chemical Exchange Saturation Transfer (CEST): what is in a name and what isn't? Mag Reson Med. 2011; 65(4):927–948.
8. Vinogradov E, He HM, Lubag A, Balschi JA, Sherry AD, Lenkinski RE. MRI detection of paramagnetic chemical exchange effects in mice kidneys in vivo. Magn Reson Med. 2007; 58(4): 650–655. [PubMed: 17899603]
9. Liepinsh E, Otting G. Proton exchange rates from amino acid side chains - Implications for image contrast. Magn Reson Med. 1996; 35(1):30–42. [PubMed: 8771020]
10. Ward KM, Aletras AH, Balaban RS. A new class of contrast agents for MRI based on proton chemical exchange dependent saturation transfer (CEST). J Magn Reson. 2000; 143(1):79–87. [PubMed: 10698648]
11. Zhang SR, Wu KC, Sherry AD. A novel pH-sensitive MRI contrast agent. Angewandte Chemie-International Edition. 1999; 38(21):3192–3194.
12. Zhang SR, Merritt M, Woessner DE, Lenkinski RE, Sherry AD. PARACEST agents: Modulating MRI contrast via water proton exchange. Acc Chem Res. 2003; 36(10):783–790. [PubMed: 14567712]
13. Woessner DE, Zhang SR, Merritt ME, Sherry AD. Numerical solution of the Bloch equations provides insights into the optimum design of PARACEST agents for MRI. Magn Reson Med. 2005; 53(4):790–799. [PubMed: 15799055]
14. Li AX, Hudson RHE, Barrett JW, Jones CK, Pasternak SH, Bartha R. Four-Pool Modeling of Proton Exchange Processes in Biological Systems in the Presence of MRI-Paramagnetic Chemical Exchange Saturation Transfer (PARACEST) Agents. Magn Reson Med. 2008; 60(5):1197–1206. [PubMed: 18958857]
15. Liu GS, Li YG, Pagel MD. Design and characterization of a new irreversible responsive PARACEST MRI contrast agent that detects nitric oxide. Magn Reson Med. 2007; 58(6):1249–1256. [PubMed: 18046705]
16. van Zijl PCM, Jones CK, Ren J, Malloy CR, Sherry AD. MRI detection of glycogen in vivo by using chemical exchange saturation transfer imaging (glycoCEST). Proc Natl Acad Sci U S A. 2007; 104(11):4359–4364. [PubMed: 17360529]
17. Ling W, Regatte RR, Navon G, Jerschow A. Assessment of glycosaminoglycan concentration in vivo by chemical exchange-dependent saturation transfer (gagCEST). Proc Natl Acad Sci U S A. 2008; 105(7):2266–2270. [PubMed: 18268341]
18. Haris M, Cai K, Singh A, Hariharan H, Reddy R. in vivo mapping of brain myo-inositol. Neuroimage. 2011; 54(3):2079–2085. [PubMed: 20951217]
19. Jin, T.; Kim, SG. Water-metabolite hydroxyl proton exchange studied using spin-locking and chemical exchange saturation transfer approaches. 2011; Montreal, Canada. Proc 19th ISMRM Annual Meeting; p. 708
20. Chan KWY, McMahon MT, Kato Y, Liu GS, Bulte JWM, Bhujwalla ZM, Artemov D, van Zijl PCM. Natural D-glucose as a biodegradable MRI contrast agent for detecting cancer. Magn Reson Med. 2012; 68(6):1764–1773. [PubMed: 23074027]
21. McMahon MT, Gilad AA, DeLiso MA, Cromer Berman SM, Bulte JWM, van Zijl PCM. New "Multicolor" Polypeptide Diamagnetic Chemical Exchange Saturation Transfer (DIACEST) Contrast Agents for MRI. Magn Reson Med. 2008; 60(4):803–812. [PubMed: 18816830]
22. Walker-Samuel S, Ramasawmy R, Torrealdea F, Rega M, Rajkumar V, Johnson SP, Richardson S, Goncalves M, Parkes H, Arstad E, Thomas D, Pedley R, Lythgoe M, Golay X. In vivo imaging of

glucose uptake and metabolism in tumors. Nat Med. 2013; 19(8):1067–1072. [PubMed: 23832090]

23. Nasrallah FA, Pages G, Kuchel PW, Golay X, Chuang KH. Imaging brain deoxyglucose uptake and metabolism by glucoCEST MRI. J Cereb Blood Flow Metab. 2013; 33(8):1270–1278. [PubMed: 23673434]
24. McMahon MT, Gilad AA, Zhou JY, Sun PZ, Bulte JWM, van Zijl PCM. Quantifying exchange rates in chemical exchange saturation transfer agents using the saturation time and saturation power dependencies of the magnetization transfer effect on the magnetic resonance imaging signal (QUEST and QUESP): pH calibration for poly-L-lysine and a starburst dendrimer. Magn Reson Med. 2006; 55(4):836–847. [PubMed: 16506187]
25. Jin T, Wang P, Zong X, Kim SG. Magnetic resonance imaging of the Amine-Proton EXchange (APEX) dependent contrast. Neuroimag. 2012; 59(2):1218–1227.
26. Cai K, Haris M, Singh A, Kogan F, Greenburg ME, Haris M, Detre J, Reddy R. Magnetic resonance imaging of glutamate. Nat Med. 2012; 18(2):302–306. [PubMed: 22270722]
27. McVicar N, Li AX, Goncalves DF, Bellyou M, Meakin SO, Prado MAM, Bartha R. Quantitative tissue pH measurement during cerebral ischemia using amine and amide concentration-independent detection (AACID) with MRI. J Cereb Blood Flow Metab. 2014; 34(4):690–698. [PubMed: 24496171]
28. Jin T, Wang P, Zong XP, Kim SG. MR imaging of the amide-proton transfer effect and the pH-insensitive nuclear overhauser effect at 9. 4 T. Magn Reson Med. 2013; 69(3):760–770. [PubMed: 22577042]
29. Jones CK, Polders D, Huang W, Zhu H, Hoogduin HJ, Zhou JY, Luijten P, Van Zijl P. in vivo three-dimensional whole-brain pulsed steady-state chemical exchange saturation transfer at 7 T. Magn Reson Med. 2012; 67(6):1579–1589. [PubMed: 22083645]
30. Jones, CK.; Huang, AJ.; van Zijl, PCM. Exchange-relayed nuclear Overhausser effect MRI. 2011; Montreal, Canada. Proc 19th ISMRM Annual Meeting; p. 2735
31. Jones CK, Huang A, Xu JD, Edden RAE, Schar M, Hua J, Oskolkov N, Zaca D, Zhou JY, McMahon MT, Pillai JJ, van Zijl PCM. Nuclear Overhauser enhancement (NOE) imaging in the human brain at 7 T. Neuroimage. 2013; 77:114–124. [PubMed: 23567889]
32. Liu D, Zhou J, Xue R, Zuo Z, An J, Wang JJ. Quantitative characterization of nuclear Overhauser enhancement and amide proton transfer effects in the human brain at 7 tesla. Magn Reson Med. 2013; 70(4):1070–1081. [PubMed: 23238951]
33. Jin T, Autio J, Obata T, Kim SG. Spin-locking versus chemical exchange saturation transfer MRI for investigating chemical exchange process between water and labile metabolite protons. Magn Reson Med. 2011; 65(5):1448–1460. [PubMed: 21500270]
34. Yuan J, Zhou JY, Ahuja AT, Jwang YX. MR chemical exchange imaging with spin-lock technique (CESL): a theoretical analysis of the Z-spectrum using a two-pool R-1 rho relaxation model beyond the fast-exchange limit. Phys Med Biol. 2012; 57(24):8185–8200. [PubMed: 23175033]
35. Zhou JY, Wilson DA, Sun PZ, Klaus JA, van Zijl PCM. Quantitative description of proton exchange processes between water and endogenous and exogenous agents for WEX, CEST, and APT experiments. Magn Reson Med. 2004; 51(5):945–952. [PubMed: 15122676]
36. Sun PZ. Simultaneous determination of labile proton concentration and exchange rate utilizing optimal RF power: Radio frequency power (RFP) dependence of chemical exchange saturation transfer (CEST) MRI. J Magn Reson. 2010; 202(2):155–161. [PubMed: 19926319]
37. Sun PZ, van Zijl PCM, Zhou JY. Optimization of the irradiation power in chemical exchange dependent saturation transfer experiments. J Magn Reson. 2005; 175(2):193–200. [PubMed: 15893487]
38. Sun PZ. Simplified quantification of labile proton concentration-weighted chemical exchange rate (k(ws)) with RF saturation time dependent ratiometric analysis (QUESTRA): Normalization of relaxation and RF irradiation spillover effects for improved quantitative chemical exchange saturation transfer (CEST) MRI. Magn Reson Med. 2012; 67(4):936–942. [PubMed: 21842497]
39. Trott O, Palmer AG. R-1rho relaxation outside of the fast-exchange limit. J Magn Reson. 2002; 154(1):157–160. [PubMed: 11820837]

40. Jin T, Kim SG. Quantitative Chemical Exchange Sensitive MRI Using Irradiation with Toggling Inversion Preparation. Magn Reson Med. 2012; 68(4):1056–1064. [PubMed: 22887701]
41. Trott O, Palmer AG. Theoretical study of R-1p rotating-frame and R-2 free-precession relaxation in the presence of n-site chemical exchange. J Magn Reson. 2004; 170(1):104–112. [PubMed: 15324763]
42. Zaiss M, Bachert P. Exchange-dependent relaxation in the rotating frame for slow and intermediate exchange - modeling off-resonant spin-lock and chemical exchange saturation transfer. NMR Biomed. 2013; 26(5):507–518. [PubMed: 23281186]
43. Lee S-P, Silva AC, Ugurbil K, Kim S-G. Diffusion-weighted spin-echo fMRI at 9. 4 T: microvascular/tissue contribution to BOLD signal change. Magn Reson Med. 1999; 42(5):919–928. [PubMed: 10542351]
44. Sun PZ, Wang EF, Cheung JS. Imaging acute ischemic tissue acidosis with pH-sensitive endogenous amide proton transfer (APT) MRI-Correction of tissue relaxation and concomitant RF irradiation effects toward mapping quantitative cerebral tissue pH. Neuroimage. 2012; 60(1):1–6. [PubMed: 22178815]
45. Kim M, Gillen J, Landman BA, Zhou JY, van Zijl PCM. Water Saturation Shift Referencing (WASSR) for Chemical Exchange Saturation Transfer (CEST) Experiments. Magn Reson Med. 2009; 61(6):1441–1450. [PubMed: 19358232]
46. Kiozumi J, Yoshida Y, Nakazawa T, Ooneda G. Experimental studies of ischemic brain edema: I: a new experimental model of cerebral embolism in rats in which recirculation can be introduced in the ischemic area. The Japanese Journal of Stroke. 1986; 8:1–8.
47. Hua J, Jones CK, Blakeley J, Smith SA, van Zijl PCM, Zhou JY. Quantitative description of the asymmetry in magnetization transfer effects around the water resonance in the human brain. Magn Reson Med. 2007; 58(4):786–793. [PubMed: 17899597]
48. Cai K, Singh A, Roalf DR, Nanga RP, Haris M, Hariharan H, Gur R, Reddy R. Mapping glutamate in subcortical brain structures using high-resolution GluCEST MRI. NMR Biomed. 2013; 26(10): 1278–1284. [PubMed: 23553932]
49. Haris M, Nath K, Cai KJ, Singh A, Crescenzi R, Kogan F, Verma G, Reddy S, Hariharan H, Melhem ER, Reddy R. Imaging of glutamate neurotransmitter alterations in Alzheimer's disease. NMR Biomed. 2013; 26(4):386–391.
50. Zong X, Wang P, Kim S-G, Jin T. Sensitivity and Source of Amine-Proton Exchange and Amide-Proton Transfer Magnetic Resonance Imaging in Cerebral Ischemia. Magn Reson Med. 2014; 71(1):118–132. [PubMed: 23401310]
51. Santyr GE, Fairbanks EJ, Kelcz F, Sorenson JA. Off-Resonance Spin Locking for Mr-Imaging. Magn Reson Med. 1994; 32(1):43–51. [PubMed: 8084236]
52. Murase K. Behavior of the magnetization in spin-locking magnetic resonance imaging using numerical solutions to the time-dependent Bloch equations. Phys Med Biol. 2012; 57:N481–N492. [PubMed: 23154187]
53. Mougin O, Clemence M, Peters A, Pitiot A, Gowland P. High-resolution imaging of magnetisation transfer and nuclear Overhauser effect in the human visual cortex at 7 T. NMR Biomed. 2013; 26(11):1508–1517. [PubMed: 23801569]
54. Sun PZ, Sorensen AG. Imaging pH using the chemical exchange saturation transfer (CEST) MRI: Correction of concomitant RF irradiation effects to quantify CEST MRI for chemical exchange rate and pH. Magn Reson Med. 2008; 60(2):390–397. [PubMed: 18666128]
55. Vinogradov E, Sherry AD, Lenkinski RE. CEST: From basic principles to applications, challenges and opportunities. J Magn Reson. 2013; 229:155–172. [PubMed: 23273841]
56. Zhou JY, Lal B, Wilson DA, Laterra J, van Zijl PCM. Amide proton transfer (APT) contrast for imaging of brain tumors. Magn Reson Med. 2003; 50(6):1120–1126. [PubMed: 14648559]
57. Jin T, Mehrens H, Hendrich K, Kim SG. Mapping brain glucose uptake with chemical exchange-sensitive spin-lock MRI. J Cereb Blood Flow Metab. 2014 in press.
58. Zu ZL, Janve VA, Xu JZ, Does MD, Gore JC, Gochberg DF. A new method for detecting exchanging amide protons using chemical exchange rotation transfer. Magn Reson Med. 2013; 69(3):637–647. [PubMed: 22505325]

59. Xu J, Yadav NN, Bar-Shir A, Jones CK, Chan KW, Zhang J, Walczak P, McMahon MT, van Zijl PCM. Variable delay multi-pulse train for fast chemical exchange saturation transfer and relayed-nuclear overhauser enhancement MRI. Magn Reson Med. 2014; 71(5):1798–1812. [PubMed: 23813483]

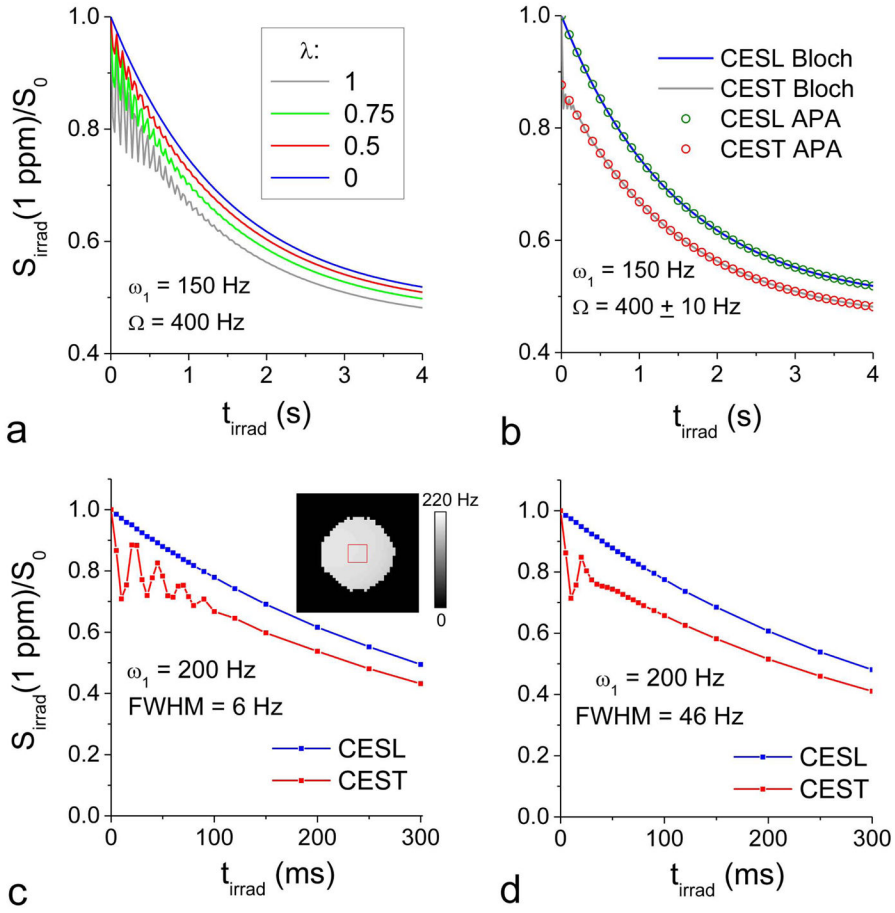

Fig. 1. Simulated and experimental signal intensities as a function of off-resonance irradiation duration

(A–B) Time-dependent signals were simulated using the Bloch-McConnell equations during off-resonance irradiation with pulse power ω_1= 150 Hz and frequency Ω = 400 Hz (i.e., 1 ppm at 9.4 T). Other parameters used were R_1 = 0.35 s^{-1}, R_2 = 3 s^{-1}, and P_S = 0. In reality, the flip of water magnetization in the SL preparation is not likely to be ideal due to imperfect B_1 and/or B_0. Thus, the impact of flip angle error (λ) to the SL signals was simulated for four different λ values (A). λ = 1 and 0 corresponds to CEST and ideal CESL, respectively. λ of 0.5 significantly reduces the signal oscillation and improves the sensitivity compared to CEST. When there is a small B_0 inhomogeneity with ±10 Hz distribution, the oscillation component of CEST vanishes quickly (gray line in B), and the simulation results of the Bloch-McConnell equations match very well with those obtained from the CE-sensitive relaxation model with asymmetric population approximation (CEAPA) solutions (circles in B). (C–D) Time-dependent saturation transfer (ST) and spin-lock (SL) data of 2% agar phantom were obtained at Ω = 400 Hz under two field shimming conditions: water spectral line width (FWHM) = 6 Hz (C) and 46 Hz (D). The ST MRI signal oscillation at short irradiation times (<100 ms) is reduced when there is larger field inhomogeneity. Inset: the ROI was overlaid on the ω_1 map. S_{irrad}: the signal intensity with off-resonance irradiation at 1 ppm; t_{irad}: off-resonance irradiation time.

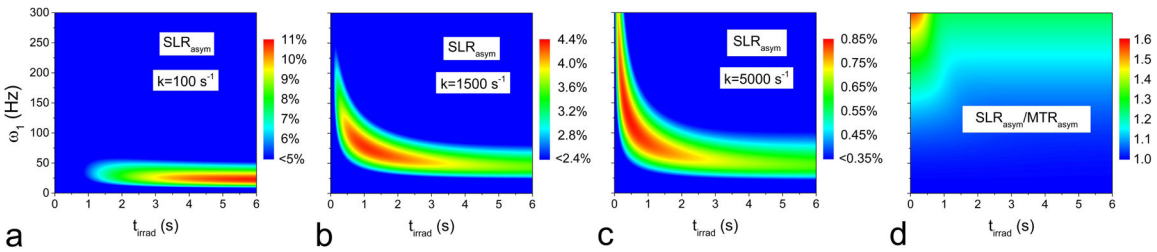

Fig. 2. Exchange rate-dependent CESL sensitivity as a function of off-resonance irradiation power and duration

SLR_{asym} as a function of ω_1 and t_{irrad} was simulated from CEAPA solutions for exchange rate k = 100 s^{-1} (A), 1500 s^{-1} (B), and 5000 s^{-1} (C), where the color bar is in units of % of S_0. The ratio of SLR_{asym} to MTR_{asym} (D) is nearly identical for all three exchange rates. Other parameters used were R_1 = 0.35 s^{-1}, R_2 = 25 s^{-1}, P_S = 0.001, and offset frequency δ = 400 Hz. Faster CE-sensitive contrast is optimal at a higher irradiation power and shorter duration (red region in C). ω_1: off-resonance irradiation power; t_{irad}: off-resonance irradiation time.

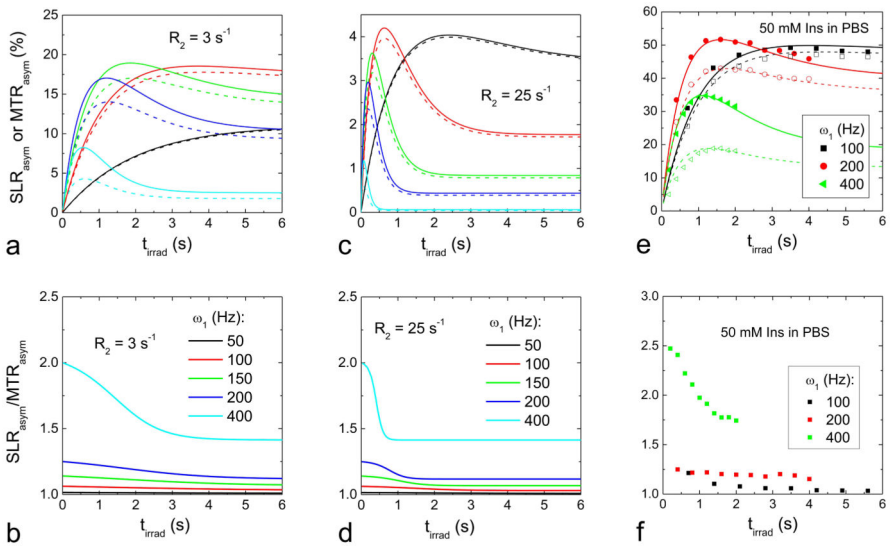

Fig. 3. Simulated and experimental CEST versus CESL contrast

(A–D) MTR_{asym} and SLR_{asym}, as a function of irradiation duration t_{irrad}, were simulated with CEAPA solutions for selected ω_1 values. Two different R_2 values were used: 3 s^{-1} (A–B) and 25 s^{-1} (C–D). SLR_{asym} (solid lines in A and C) is always larger than MTR_{asym} (dashed lines), but the difference is more significant at higher ω_1 and shorter t_{irrad} values. The ratio of SLR_{asym} to MTR_{asym} (B and D) ranges between $1/\cos^2\theta$ at very short t_{irrad} and $1/\cos\theta$ at long t_{irrad}, approaching the steady state. Other parameters used were R_1 = 0.35 s^{-1}, P_S = 0.001, and δ = 400 Hz. (E–F) MTR_{asym} (open symbols) and SLR_{asym} (filled symbols) of 50 mM myo-inositol (Ins) in PBS were measured at 1 ppm with ω_1 = 100, 200, and 400 Hz at varying irradiation durations (E), and their ratios were obtained (F). For the highest ω_1 of 400 Hz, we only acquired t_{irrad} up to 2 s to minimize RF heating in the samples. MTR_{asym} and SLR_{asym} peaks shift to shorter t_{irrad} at higher ω_1. The ratio between SLR_{asym} and MTR_{asym} increases with ω_1 and is larger at shorter irradiation times (F). To verify the experimental data with CEAPA models, on-resonance spin-locking experiments as a function of ω_1 were performed, and chemical exchange parameters were obtained (see texts). Simulated MTR_{asym} and SLR_{asym} data (lines in E) using these chemical exchange parameters match well with the experimental data (symbols in E). t_{irad}: off-resonance irradiation time.

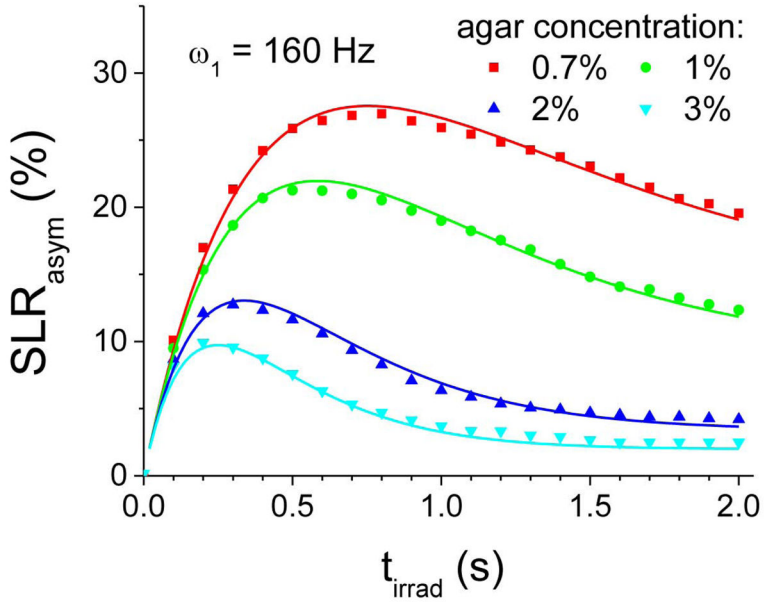

Fig. 4. Experimental vs. simulated CESL signal of tissue-mimicking phantoms

SLR_{asym} data of 50 mM myo-inositol (Ins) in 0.7%, 1%, 2%, and 3% agar were obtained with a ω_1 of 160 Hz. SLR_{asym} data were also simulated by the CEAPA models with chemical exchange parameters (see texts). The measured SLR_{asym} data of Ins phantoms (symbols) can be well explained by the simulated data by the CEAPA models (solid lines), indicating that analytical CEAPA can be applied for quantitative models of CE-MRI. t_{irad}: off-resonance irradiation time.

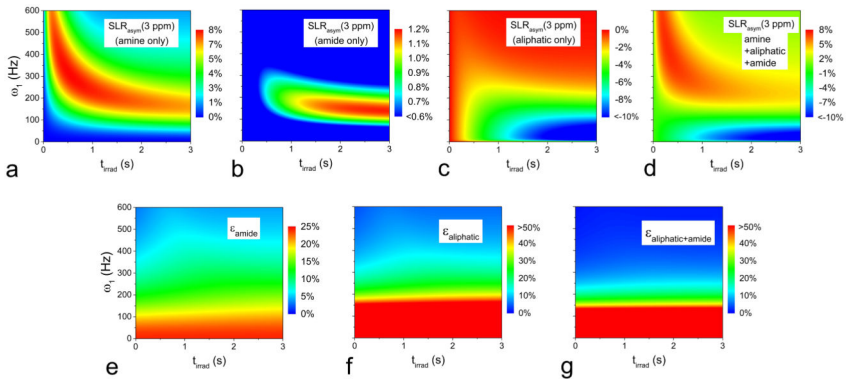

Fig. 5. Selectivity of amine CESL MRI increases with high irradiation power: simulations

SLR_{asym} as a function of ω_1 and t_{irrad} was simulated at an off-resonance frequency 3 ppm (i.e., 1200 Hz) from CEAPA solutions for amine pool only with population P_{amine} = 0.0012, exchange rate k_{amine} = 7500 s^{-1}, and chemical resonance frequency δ_{amine} = 1200 Hz (A); amide pool only with P_{amide} = 0.0012, k_{amide} = 30 s^{-1}, and δ_{amide} = 1400 Hz (B); aliphatic pool only with $P_{aliphatic}$ = 0.003, $k_{aliphatic}$ = 20 s^{-1}, and $\delta_{aliphatic}$ = −1200 Hz (C); and all three pools together (D), where the color bar is in units of % of S_0. The contamination of slow exchanging protons to the amine signal — *i.e.*, $\varepsilon = |SLR_{asym}(\text{non-amine})|/SLR_{asym}(\text{amine})$ — was shown as a percentage in (E) for amide pool only, (F) for aliphatic pool only, and (G) for the combination of amide and aliphatic pools. ω_1: off-resonance irradiation power; t_{irad}: off-resonance irradiation time.

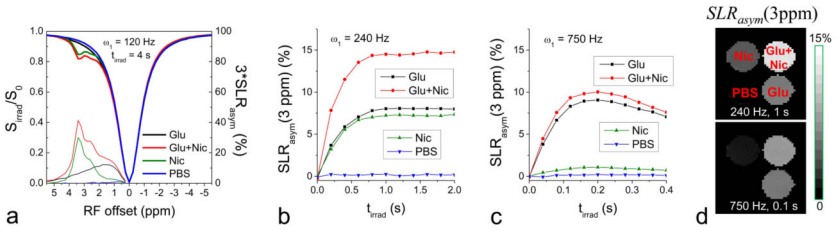

Fig. 6. Selectivity of amine CESL MRI increases with high irradiation power: phantom experiments at room temperature

CESL experiments were performed at various experimental parameters for 30 mM glutamate (Glu), 200 mM nicotinamide (Nic), 30 mM Glu plus 200 mM Nic, and PBS phantoms. (A) Z-spectra (thick) and 3-times amplified SLR_{asym} (thin) measured with a low power of ω_1 = 120 Hz and t_{irrad} = 4 s show that amine-CESL signals are overlapping with that of amide. (B–C) SLR_{asym} at 3 ppm was calculated as a function of t_{irrad} for a medium power ω_1 = 240 Hz (B) and a high power of 750 Hz (C). With 240 Hz, Glu (black) and Nic (green) signals are similar and reach a peak at t_{irrad} > 1 s. With 750 Hz, the Glu signal reaches a peak at t_{irrad} <0.2 s, where the Nic SLR_{asym} is minimized. The enhancement of amine selectivity is also shown in the SLR_{asym} map (D) obtained with ω_1 = 750 Hz and t_{irrad} = 0.1 s. ω_1: off-resonance irradiation power; t_{irad}: off-resonance irradiation time

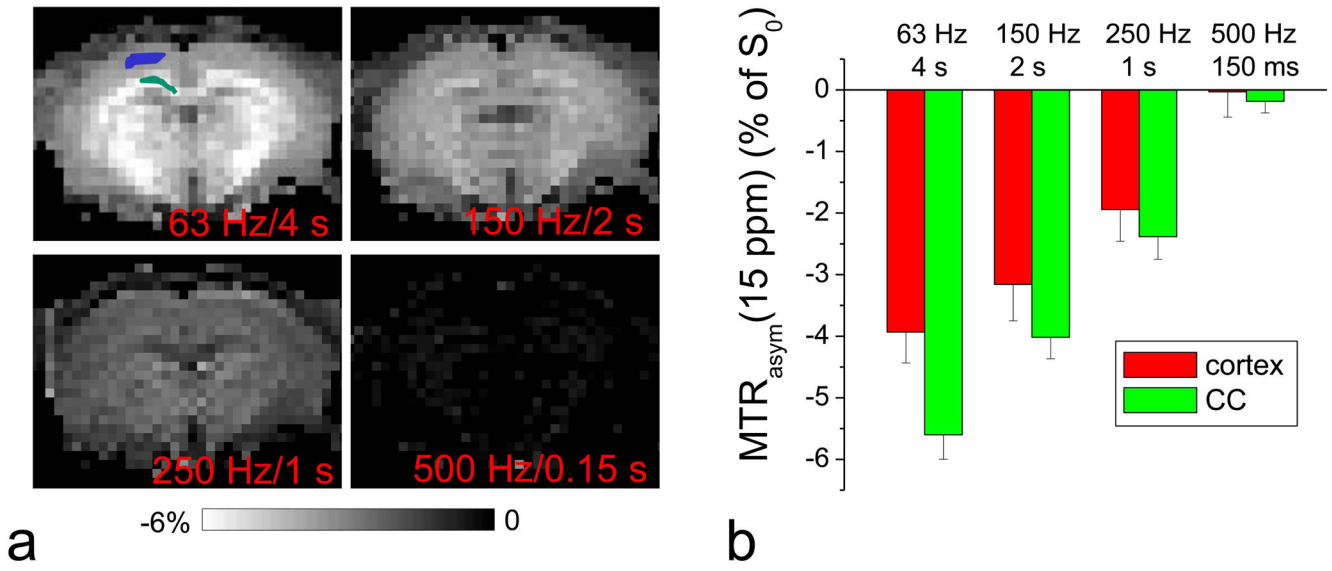

Fig. 7. Dependence of *in vivo* asymmetric MTC effect on irradiation parameters

In vivo MTR_{asym} of rat brains was measured at an RF offset of 15 ppm with four different irradiation power and duration pairs. Maps of one representative animal are shown (A), and the averaged MTR_{asym} (n = 6 rats) was calculated from the cortex (blue pixels in A) and corpus callosum (CC, green pixels) ROIs (B). The asymmetric MTC is higher in the white matter than in gray matter and decreases with a higher irradiation power and shorter duration condition.

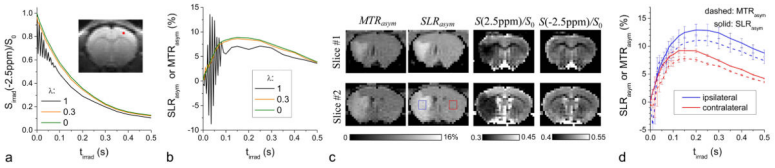

Fig. 8. ***In vivo*** **amine-water proton exchange (APEX) signals measured with CEST and CESL**

CEST and CESL MRI of rat brains were measured with RF offsets of ±2.5 ppm and ω_1 of 500 Hz. (A–B) Data of a single pixel (inset in A) were examined with different flip angle error λ (=1 for CEST and 0 for CESL). The CEST signal intensity at −2.5 ppm and MTR_{asym} (black lines) oscillate for short t_{irrad}. Similar to the simulation and phantom studies, the *in vivo* results with flip angle error λ = 0.3 are already close to those of ideal spin-lock with λ = 0 and have higher sensitivity than saturation transfer with λ = 1. (C) In ischemic rats, the MTR_{asym} and SLR_{asym} maps with t_{irrad} = 0.15 s show similar ischemic contrast, but the latter has about 20% higher sensitivity. While SLR_{asym} maps are calculated from the difference of two normalized maps of S/S_0 at ± 2.5 ppm, this ischemic contrast mostly originates from the APEX-weighted signal at 2.5 ppm. Note the difference gray scales of the maps. (D) The averaged MTR_{asym} and SLR_{asym} (n = 4) as a function of t_{irrad} were obtained from the 2×2 mm^2 ROIs in the ischemic ipsilateral (blue) and normal contralateral sides (red box). The CESL SLR_{asym} signal (solid) has higher sensitivity and higher ischemic contrast (red vs. blue) than CEST MTR_{asym} (dashed).